INL/EXT-09-17084

High Repetition Rate, LINAC-Based Nuclear Resonance Fluorescence FY 2009 Final Report

Mathew Kinlaw
Scott Watson
James Johnson
Alan Hunt
Heather Seipel
Edward Reedy

October 2009

The INL is a U.S. Department of Energy National Laboratory
operated by Battelle Energy Alliance

INL/EXT-09-17084

High Repetition Rate, LINAC-Based Nuclear Resonance Fluorescence FY 2009 Final Report

Mathew Kinlaw
Scott Watson
James Johnson
Alan Hunt[1]
Heather Seipel[1]
Edward Reedy[1]

[1]Idaho State University

October 2009

Idaho National Laboratory
Idaho Falls, Idaho 83415

http://www.inl.gov

Prepared for the
U.S. Department of Energy
Office of NA-22
Under DOE Idaho Operations Office
Contract DE-AC07-05ID14517

SUMMARY

Nuclear Resonance Fluorescence (NRF), which is possible for nuclei with atomic numbers greater than helium (Z=2), occurs when a nuclear level is excited by resonant absorption of a photon and subsequently decays by reemission of a photon [1]. The excited nuclear states can become readily populated, provided the incident photon's energy is within the Doppler-broadened width of the energy level being excited. Utilizing continuous energy photon spectra, as is characteristic of a bremsstrahlung photon beam, as the inspection source, ensures that at least some fraction of the impinging beam will contribute to the population of the excited energy levels in the material of interest. Upon de-excitation, either to the ground state or to a lower-energy excited state, the emitted fluorescence photon's energy will correspond to the energy difference between the excited state and the state to which it decays. As each isotope inherently contains unique nuclear energy levels, the NRF states for each isotope are also unique. By exploiting this phenomenon, NRF photon detection provides a well-defined signature for identifying the presence of individual nuclear species.

This report summarizes the second year (Fiscal Year [FY] 2009) of a collaborative research effort between Idaho National Laboratory, Idaho State University's Idaho Accelerator Center, and Pacific Northwest National Laboratory. This effort focused on continuing to assess and optimize NRF-based detection techniques utilizing a slightly modified, commercially available, pulsed medical electron accelerator. During the course of FY 2008, a gain shift occurred in some data sets, resulting from radiofrequency (RF) pickup and the existence of substantial ground loops in the accelerator control system. This pickup was addressed and subsequently eliminated by replacing the legacy cables with single run signal cables, which also contained improved cable shielding. Ground loops were eliminated through an optical isolation of the data acquisition system from the accelerator control system. Overall, the RF pickup was decreased by more than a factor of 100. The FY 2009 testing configurations were further optimized with the identification and acquisition of a more appropriate nuclear material target (0.22 cm thick ^{238}U), which provided a significant increase in the signal-to-background ratio and decrease in the time necessary to detect both nuclear and non-nuclear material in the presence of high-Z material.

A primary focus for FY 2009 tasking included modifying/upgrading the current LINAC to support NRF operations with accelerator repetition rates up to 2 kHz. By increasing the capacitance and inductance of the pulse forming network and changing the RF driver to a long pulse mode, the LINAC's RF pulse width was extended to 20 μs. With the construction of a new electron gun hot deck and burst mode pulsing system, multiple electron pulses were available for injection during a single RF pulse. This multipulse capability, in conjunction with an RF repetition rate of 300 Hz, produced an effective bremsstrahlung repetition rate of up to 3 kHz. Furthermore, with this increased repetition rate capability, the previously utilized data acquisition system also required improvements. The spectroscopy amplifier was replaced by a gated integrator with 2.3 μs wide (full width at half maximum [FWHM]) output pulses; the gated integrator was ~5.2 times faster than the previous spectroscopy amplifier. A fixed conversion time analog-to-digital convertor (ADC) was added, which, with a 900 ns conversion time, was 47 times faster than the previously utilized Wilkinson

ADC. Subsequent measurements (with a 3 kHz repetition rate) demonstrated significant improvements in the signal-to-background ratios, particularly with respect to high-Z and/or nuclear material targets. The detection of ^{238}U transition rates also improved, providing a 37% increase in statistical confidence compared to previous efforts.

In conclusion, both the LINAC and data acquisition systems were modified to operate with an accelerator repetition rate up to 3000 Hz. Successful NRF measurements were performed on several non-nuclear targets with both low and high atomic numbers. The NRF measurements performed with nuclear material (^{238}U) were significantly improved from previous efforts. Based on FY 2009 experimental results, a clear path-forward has been developed to include a further examination of the effects of pulse pileup, continue to increase the overall rate of data acquisition, and begin preliminary assessments for additional target materials (^{235}U).

CONTENTS

FIGURES

TABLES

ACRONYMS

ADC	analog-to-digital convertor
DHS	Department of Homeland Security
DNDO	Domestic Nuclear Detection Office
DOE	Department of Energy
FWHM	full width at half maximum
FY	Fiscal Year
IAC	Idaho Accelerator Center
INL	Idaho National Laboratory
NRF	Nuclear Resonance Fluorescence
PNNL	Pacific Northwest National Laboratory
RF	radiofrequency

High Repetition Rate, LINAC-based Nuclear Resonance Fluorescence FY 2009 Final Report

1. INTRODUCTION

This report summarizes the second year of a multi-laboratory/university, multi-year effort focusing on increasingly high-repetition rate, pulsed LINAC-based nuclear resonance fluorescence (NRF) measurements. The FY 2009 effort continued to assess the viability of utilizing pulsed linear electron accelerators for the isotopic identification of various nuclear and non-nuclear targets. In the recent past, the Department of Homeland Security (DHS) and the Department of Energy (DOE/NA-22), among others, have expressed interest in examining NRF's reliability as a competing nuclear material detection technology. Such interests have traditionally relied upon continuous-wave, Van de Graff bremsstrahlung sources to provide the inspection beam. However, the present-day use of Van de Graff sources with electron acceleration columns is becoming increasingly limited and only selected NRF data from special nuclear materials has been presented.

An inspection system designed to detect specific materials of interest must be able to precisely and accurately identify these materials, whether they be special nuclear material, explosives, or other illicit materials. While passive detection systems can provide isotope specificity by identifying unique gamma-ray and/or neutron signatures, most have insufficient sensitivity for positively detecting and identifying target materials in the presence of shielding. Alternative inspection systems based upon conventional x-rays, including standard gamma-ray imagers, typically lack the ability to discriminate between nuclear materials and other non-threatening targets comprised of high-Z materials. As a result, electron accelerator-based NRF is being studied as a method that can provide both sensitivity and isotope identification for detecting and identifying nuclear material.

This collaborative effort between Idaho National Laboratory (INL), Idaho State University's Idaho Accelerator Center (IAC), and Pacific Northwest National Laboratory (PNNL) continues to advance the understanding and assess the efficacy of utilizing conventional, commercially available LINACs for NRF measurements. Building upon FY 2008 research, this FY 2009 work continued to examine experimental configurations for optimal NRF measurements and testing with both nuclear and non-nuclear materials. Fundamental modifications were applied to both the LINAC and data acquisition systems, providing an increased capability for operations with effective bremsstrahlung repetition rates up to 3 kHz. Subsequent NRF measurements performed on both non-nuclear and nuclear materials were quite successful, including a 37% increase in the statistical confidence for the detection of ^{238}U NRF transitions.

2. BACKGROUND

Idaho National Laboratory (INL), in conjunction with Idaho State University's IAC, continues to develop accelerator-based active interrogation technologies, continuing nearly two decades of collaborative accelerator-based detection research [4]. Such efforts have contributed to the development of multiple applications in support of the Department of Energy's Office of Nonproliferation and National Security (NA-22), the DHS Domestic Nuclear Detection Office (DNDO), and other various governmental agencies. For over a decade, INL has exploited gamma-ray emissions for detecting and identifying nuclear and/or explosive materials [5–8]. Furthermore, INL and the IAC have developed several techniques that utilize active inspection methodologies to induce and detect unique radiation signatures from nuclear materials and other illicit contraband. The time-dependence of delayed neutron emission has been demonstrated for isotope identification, while other photonuclear inspection techniques have been utilized to detect 100 kg of explosives contained in an automobile [8, 10, 11]. The Pulsed Photonuclear Assessment technology has a demonstrated ability of detecting shielded nuclear material at distances exceeding 100 m, with outdoor testing rapidly extending this standoff capability [5, 12–14].

Nuclear Resonance Fluorescence (NRF) occurs in all nuclei with atomic numbers greater than two, due to the presence of unique and well-defined nuclear states [2, 3]. Population of the excited states, which are several MeV above the ground states, can occur as a result of the nuclei absorbing specific-energy photons, followed by the emission of discrete energy photons (fluorescence). Exploiting the continuous energy spectrum inherent with bremsstrahlung radiation ensures at least some portion of the impinging inspection photon beam is within the energy range for inducing NRF transitions within the target of interest. Additionally, these energy levels are unique to each isotope; hence, the energies of the resulting NRF-produced photons are unique as well. Therefore, Nuclear Resonance Fluorescence is a promising and attractive method for detecting and identifying the presence of specific isotopes.

Traditionally, NRF research has been reliant upon continuous-wave, Van de Graff-based bremsstrahlung sources. However, very few Van de Graff sources with electron acceleration columns are still in use and only limited NRF data from special nuclear materials has been presented. The research presented here, which is in its second year, focuses on experimentally assessing the efficacy of performing NRF measurements using conventional, commercially-available pulsed electron accelerators.

3. OPTIMIZING NRF MEASUREMENTS

Building upon the FY 2008 experimental results, FY 2009 efforts sought to immediately address the most significant of the challenges identified during FY 2008. Substantial noise was observed in the data acquisition system as a result of RF pickup during the 1 kHz operations [9]. This RF noise was producing gain shifts in the detected spectra, requiring application of post-processing algorithms to recombine the data. Furthermore, the identification of NRF transitions with small integrated cross sections was problematic in cases where high-Z materials were included in the target. Hence, continued experimental optimization was recommended to stabilize data acquisition, reduce the active background, and increase the signal-to-noise ratio for high-Z and/or nuclear material targets.

3.1 Reducing Radiofrequency Noise Pickup

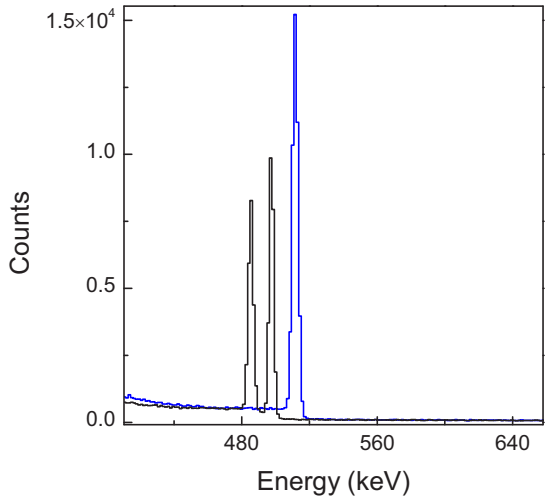

Figure 1. Gain shifting from radiofrequency noise pickup. The two black peaks are gain-shifted 511 keV peaks, while the blue peak represents the 511 keV peak following application of post-processing gain stabilization software.

A significant challenge was identified in FY 2008 in terms of the production of substantial gain shifts in the gamma-ray energy spectra during lengthy runs. This shifting was determined to be a result of the introduction of radiofrequency (RF) noise into the detector and data acquisition electronics. Figure 1 presents an example of the gain shifting of the 511 keV peak due to RF pickup. The two black peaks are both 511 keV peaks from the detection of positron annihilation gamma-rays. At some point during data acquisition, RF noise pickup produced the noticeable shift in the gain, subsequently shifting the gamma-ray peaks. To compensate for this undesired effect, software was written to apply a gain stabilizing algorithm to the data, the result of which can be seen as the blue 511 keV peak in Figure 1. However, to minimize the opportunity for RF noise to interfere with the detector or acquisition system, several modifications were applied to various system components, including a differential output capability on the HPGe detector. Legacy signal cables utilized during past data collection were replaced with single-run, double-shielded signal cables. It was also determined that considerable ground loops were present in the system. To reduce their effect, as well as minimize any RF pickup generated from the LINAC gun trigger that is necessary for use by the data acquisition system, the acquisition system was electrically isolated from the gun trigger. Essentially, the signal from the gun trigger was passed to an electrical-to-optical converter. A fiber optic cable brought the signal to the data acquisition system, where the optical signal was converted back to an electrical signal. Figure 2 shows the signals prior to and after the

modifications were applied. The red line is the original RF noise produced from the ground loops with the accelerator controls, while the black line is the signal following the isolation of the accelerator controls. Overall, the modifications reduced the RF noise pickup in the acquisition system by a factor of more than 100.

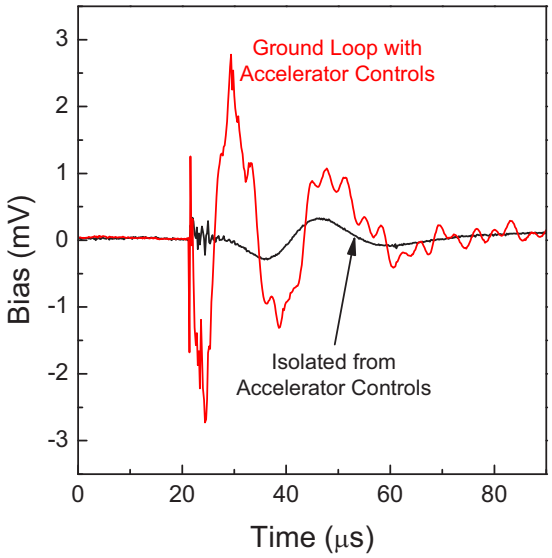

Figure 2. Pre and post-system modifications for minimizing RF noise pickup. The signal was improved by a factor of more than 100, resulting from enhanced signal cables, the elimination of ground loops with the accelerator control system, and the addition of differential signal amplification.

3.2 Signal-to-Background Ratios versus Counts per Pulse

Continuing to optimize the experimental configurations and corresponding NRF measurements, several data sets were collected that examined how the signal-to-background ratio varied as a function of total counts per bremsstrahlung pulse. Figure 3 compares the gamma-ray spectra from a 0.317 cm ^{nat}Pb target irradiated with a 360 Hz, 6 MeV endpoint energy bremsstrahlung beam. The black data correspond to a total count rate of 0.20 counts per bremsstrahlung pulse, while the red data represent a total count rate of 0.34 counts per bremsstrahlung pulse. As expected, there is a visually noticeable increase in the total number of counts for the 0.34 counts per pulse data versus the 0.20 counts per pulse data, especially with respect to the NRF lines from the Pb target. Figure 4 compares the time-averaged count rates for the 4.842 and 5.513 MeV NRF transitions from ^{208}Pb. Due to pulse pileup, Poisson statistics suggest a ~50% increase in the count rate when increasing the total counts per pulse from 0.20 to 0.33. Based on the 0.20 counts per pulse data, the NRF transition rates for the 0.33 counts per pulse data were expected to be 33.9 $\times 10^{-7}$ and 34.1 $\times 10^{-7}$ per pulse for the 5.513 and 4.842 MeV transitions, respectively. However, the observed average count rates were only 28 $\times 10^{-7}$ and 20 $\times 10^{-7}$ per pulse. The presence of such large statistical uncertainties makes it difficult to discern whether this trend is real or simply a function of poor counting statistics.

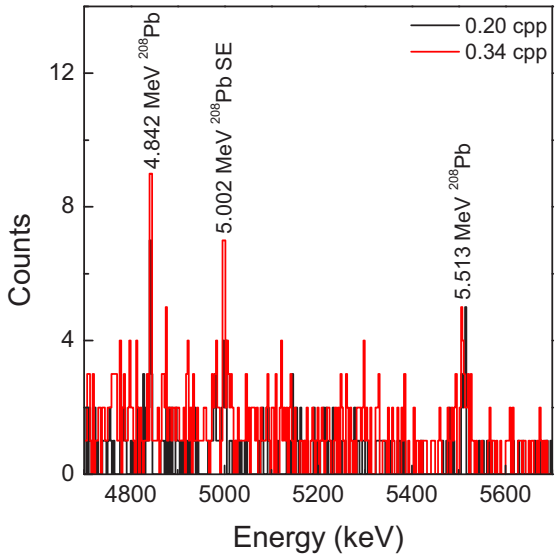

Figure 3. Comparison of gamma-ray spectra for two detected events count rates (0.20 and 0.34 counts per bremsstrahlung pulse) for a 0.317 cm Pb target. The target was irradiated with a 6 MeV endpoint energy bremsstrahlung beam, pulsed at a repetition rate of 360 Hz.

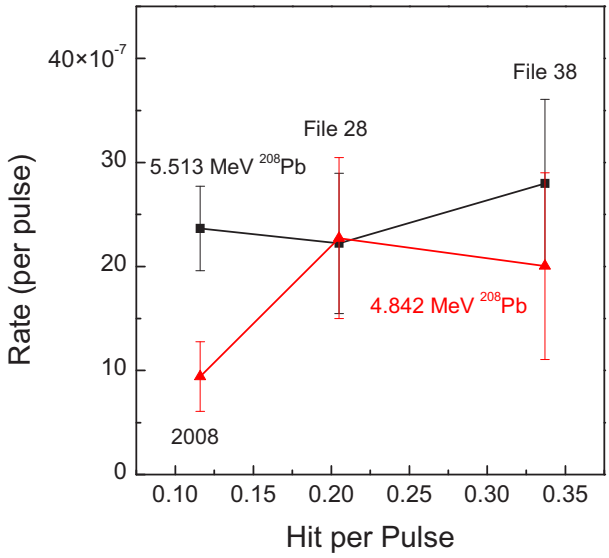

Figure 4. Comparison of the time-averaged count rates for the 4.842 and 5.513 MeV NRF transitions from the Pb target. The change in detection rate as a function of increasing the total counts per pulse is somewhat inconsistent with predictions based on Poisson statistics. These inconsistencies may be explained, at least in part, by the relatively large statistical uncertainties.

Figure 5 compares the signal-to-background ratios versus counts per bremsstrahlung pulse. The ratio was calculated by dividing the number of counts in the background-subtracted NRF line by the background counts, which were determined by side bands. As is clearly seen in Figure 5, increasing the total counts per bremsstrahlung pulse produces a significant decrease in the signal-to-background ratio for the NRF transitions. Certainly, this expected characteristic of increasing the total counting rate makes it much more challenging to identify NRF peaks above background, especially with less-probable transitions such as those expected from nuclear material.

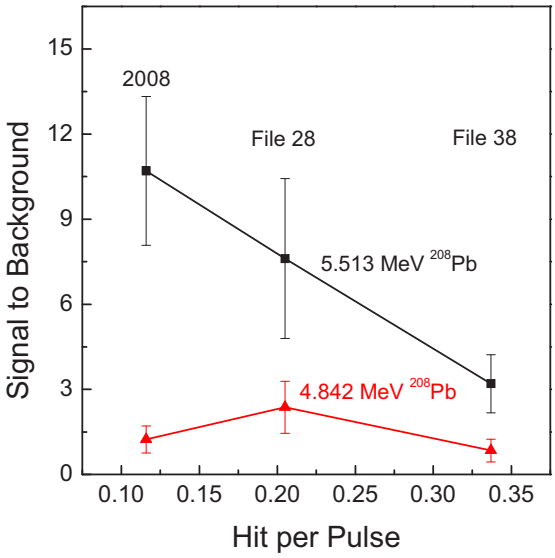

Figure 5. Comparison of signal-to-background ratios versus counts per bremsstrahlung pulse. The signal-to-background ratio decreases significantly with an increase in the total counts per bremsstrahlung pulse.

3.3 Calculating Optimal Target Thicknesses

Figure 6 shows the gamma-ray spectra from two separate targets, both irradiated with a 3.3 MeV endpoint energy bremsstrahlung beam (360 Hz repetition rate). The black data were collected from a target consisting of a 5.08 cm diameter, 0.635 cm thick boron disk and a 10.16 cm square, 0.847 cm thick depleted uranium plate. The red data were collected separately with only the boron disk. When only the boron disk was irradiated, the 2.124 MeV transition from ^{11}B is clearly visible and there is very little background, as was expected. However, with the introduction of a high-Z target, in this case depleted uranium, the ^{11}B transition is essentially lost in the elevated background. Furthermore, there was approximately the same number of ^{238}U and ^{11}B nuclei in the beam (~1.8×10^{24} and ~1.3×10^{24}, respectively) and the integrated cross sections from the two isotopes are comparable. In the absence of an elevated background, it is expected that the strength of the ^{11}B and ^{238}U NRF lines should be comparable. Hence, it is reasonable to conclude that the relatively high background rate is also contributing to the lack of visibility of the ^{238}U transitions. This highlighted the necessity to obtain and utilize a ^{238}U target with a more optimal thickness relative to the desired NRF transitions' signal-to-background ratios.

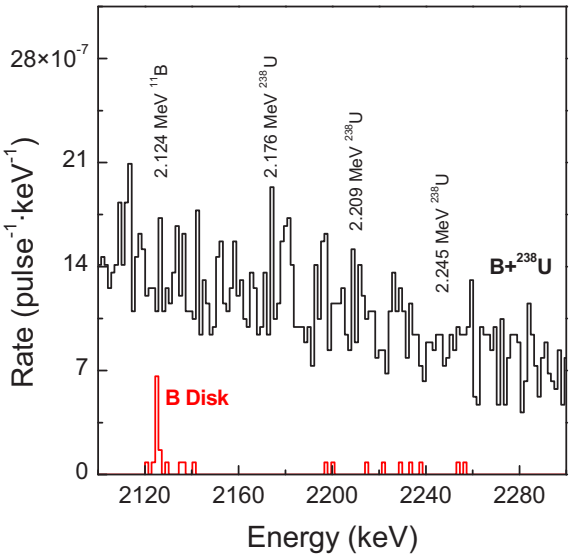

Figure 6. Gamma-ray spectra from a combined $^{11}B/^{238}U$ target (black line) and ^{11}B target (red line), irradiated with 3.3 MeV bremsstrahlung. The NRF transitions of interest are labeled.

The cross section for resonance fluorescence (resonance scattering) is

$$\sigma_0(E) = \pi \cdot \left(\lambda_{bar}\right)^2 \cdot \frac{2 \cdot J_1 + 1}{2 \cdot \left(2 \cdot J_0 + 1\right)} \cdot \frac{\Gamma_0^{\,2}}{\left(E - E_r\right)^2 + \frac{1}{4} \cdot \Gamma_T^{\,2}} \,, \tag{1}$$

where J_1 and J_0 are the total angular momentum of the excited state and ground state, respectively, E_r is the resonance energy, λ_{bar} is the wavelength (corresponding to E_r) divided by 2π, Γ_0 is the partial width for the transition of interest, and Γ_T is the total width of the excited level [15]. Then, the Doppler-broadened cross section for resonance fluorescence is

$$\sigma_{sc}(E) = \sigma_0\left(E_r\right) \cdot \psi\left[\frac{2 \cdot \left(E - E_r\right)}{\Gamma_T}\right] , \tag{2}$$

with

$$\psi(x) = \left[\frac{1}{2 \cdot (\pi \cdot t)^{\frac{1}{2}}}\right] \cdot \int_{-\infty}^{\infty} \frac{e^{\left(\frac{-u^2}{4 \cdot t}\right)}}{1 + (x - u)^2} \, du \,, \tag{3}$$

$$t = \left(\frac{\Delta}{\Gamma_T}\right)^2 \text{ and } \Delta = \left(\frac{E_r}{c}\right)\cdot\left(\frac{2\cdot k_b\cdot T_r}{M_n}\right)^{\frac{1}{2}} , \tag{4}$$

where k_b is Boltzmann's constant, T_r is the absolute temperature of the target, and M_n is the mass of the nuclei. The differential scattering rate, assuming a small volume element in which the bremsstrahlung flux is constant, is given by

$$dR = f_{nrf}\cdot n_n\cdot\frac{d\Phi}{dE}\cdot\sigma_{sc}(E)\cdot dx'dy'dz'dE , \tag{5}$$

where f_{nrf} is the fraction of nuclei that can resonantly fluoresce, n_n is the number density of the target nuclei, and $d\Phi/dE$ is the differential photon flux, which will be exponentially absorbed by the target as a function of depth (dz). In addition to resonant absorption, electronic absorption will also contribute. The resonant absorption cross section can be represented by (see [15])

$$\sigma_{0abs}(E) = \pi\cdot\left(\lambda_{bar}\right)^2\cdot\frac{2\cdot J_1+1}{2\cdot\left(2\cdot J_0+1\right)}\cdot\frac{\Gamma_0\cdot\Gamma_T}{\left(E-E_r\right)^2+\frac{1}{4}\cdot\Gamma_T{}^2} , \tag{6}$$

which leads to

$$\sigma_{abs}(E) = \sigma_{0abs}\left(E_r\right)\cdot\psi\left[\frac{2\cdot\left(E-E_r\right)}{\Gamma_T}\right] . \tag{7}$$

The differential photon flux at depth z in the target can then be expressed by

$$\frac{d\Phi}{dE} = \left.\frac{d\Phi}{dE}\right|_{z=0} e^{-n_n\cdot\left(f_{nrf}\cdot\sigma_{abs}(E)+\sigma_e(E)\right)\cdot z} , \tag{8}$$

where $\sigma_e(E)$ is the cross section for electronic absorption. Making the assumption that the integrals with respect to dx and dy in Equation (5) simply give the area of the beam spot or the target, whichever is smaller, performing the integration for dR with respect to dz and letting z go to infinity gives the yield for an infinitely thick target as

$$R_{inf} = f_{nrf}\cdot A\left.\frac{d\Phi}{dE}\right|_{z=0}\int\frac{\sigma_{sc}(E)}{f_{nrf}\cdot\sigma_{ab}(E)+\sigma_e(E)}\,dE , \tag{9}$$

where A is the area of the photon beam or target. The relative yield for a target of finite thickness is then

$$Y_{nrf} = \frac{1}{R_{inf}} f_{nrf} \cdot A \left. \frac{d\Phi}{dE} \right|_{z=0} \int \frac{\sigma_{sc}(E)}{f_{nrf} \cdot \sigma_{ab}(E) + \sigma_e(E)} \cdot \left[1 - e^{-n_t \cdot \left(f_{nrf} \cdot \sigma_{abs}(E) + \sigma_e(E) \right) \cdot z} \right] dE \quad . \qquad (10)$$

Figure 7 compares the cross section for resonance absorption and the corresponding Doppler broadened cross section as a function of variation in energy from the 2.209 MeV ^{238}U transition. As can be seen in Figure 7, the cross sections are essentially zero for incident gamma-ray energies that are greater than ±9 eV from the 2.209 MeV transition for ^{238}U. Hence, the integral contained in Equation (10) can be set equal to zero everywhere except for the region $E_r \pm \delta E$, where $\delta E = 9$ eV.[a] With this understanding, the yield [Equation (10)] can then be calculated and is shown in Figure 8.

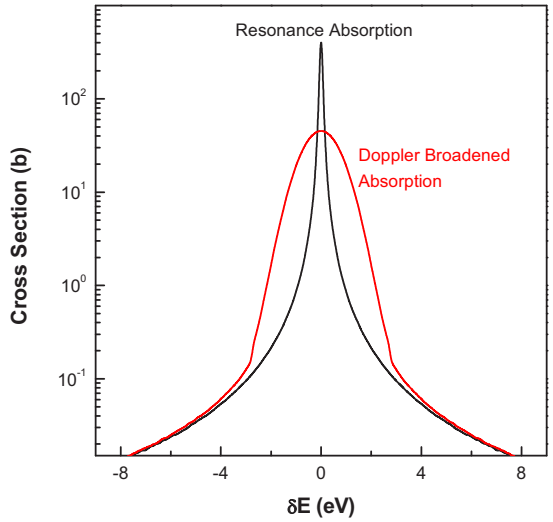

Figure 7. Comparison of the cross sections for resonance absorption and the corresponding Doppler broadened cross section as a function of variation in energy from the 2.209 MeV resonance in ^{238}U. The values of the two cross sections are essentially zero for incident gamma-ray energies that are more than ± 9 eV from the transition level.

Similar yield calculations for the 2.124 MeV transition in ^{11}B are also included, as well as relative background yields for both isotopes. While the 2.209 and 2.124 MeV transitions from ^{238}U and ^{11}B, respectively, have integrated NRF cross sections that are both ~52 b·eV, the resonance absorption cross section for the ^{238}U transition is ~1.7 times larger than the absorption cross section for the ^{11}B transition (~88 b·eV versus ~52 b·eV). As a result, the relative yield for the ^{238}U transition will saturate more quickly than the ^{11}B transition. Figure 8 also shows the relative background yield increasing as a function of thickness more quickly than the NRF yield.

a. This value relates only to the 2.209 MeV transition in ^{238}U, which will be used for determining the optimal depleted uranium target thickness. Certainly, targets comprised of alternative isotopes would require separate calculations.

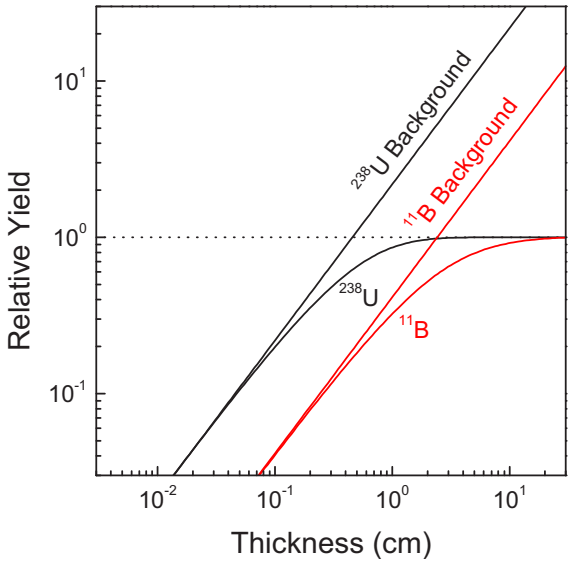

Figure 8. Comparisons of the NRF yields for ^{238}U (2.209 MeV) and ^{11}B (2.124 MeV) versus background as a function of target thickness.

Previous experimental efforts utilized ^{238}U targets that were 10.16 × 10.16 cm plates, with thicknesses varying from 0.85 to 2.54 cm. To obtain the best signal-to-background ratio, the optimal thickness should be sought for which the yield is as close to linear with thickness as possible. The thinnest target used previously (0.85 cm) produces an empirical yield that is 81% of the saturated yield, while the thickest (2.54 cm) produces a yield that is 98% of the saturated yield. Even for the 0.85 cm thick target, this yield deviates substantially from linearity. Hence, it was determined that follow-on efforts should utilize a significantly thinner ^{238}U target; a 0.216 cm target was acquired for subsequent experiments. If the background yield is assumed to increase linearly with target thickness, decreasing the target thickness by a factor of 3.9 should also decrease the background yield by a factor of 3.9. However, the NRF yield should only be decreased by a factor of 2.2; the signal-to-background ratio should improve by a factor of 1.7.

3.4 NRF Measurements

With the acquisition of the thinner ^{238}U target, the previous measurements (see Section 3.3, Figure 6) were repeated. The combined target consisted of the 5.08 cm diameter, 0.635 cm thick boron disk and a 10.16 cm square, 0.216 cm thick depleted uranium plate. The accelerator was operated at ~3 MeV, with a repetition rate of 900 Hz. As before, two data sets were collected: one with the combined target and one with only the boron disk. Figure 9 presents the results of these two runs, where the black data are from the boron target, alone, and the red data are from the combined target. As before, the 2.124 MeV transition from ^{11}B is clearly visible with little background present for only the boron disk. Contrary to previous data sets, the 2.124 MeV transition from ^{11}B is also clearly visible in the combined target data set. Up to this point, this represented the most definitive identification of a relatively small integrated cross-section NRF transition (~52 b·eV) in the presence of a high-Z material. This may be attributable, at least in part, to the utilization of the thinner ^{238}U target and the corresponding reduction in background signal. However, the ^{238}U NRF transitions (2.176 and 2.209 MeV) in the same region are not clearly visible in this data set, despite having almost identical integrated cross sections compared with the 2.124 MeV ^{11}B transition. Furthermore, the number of nuclei in the targets was comparable, with 1.35×10^{24} nuclei in the ^{11}B target and 1.193×10^{24} nuclei in the ^{238}U target. It is quite possible that the areal dimensions of the

depleted uranium plate were larger than the bremsstrahlung beam spot and a significant number of uranium nuclei were not directly irradiated.

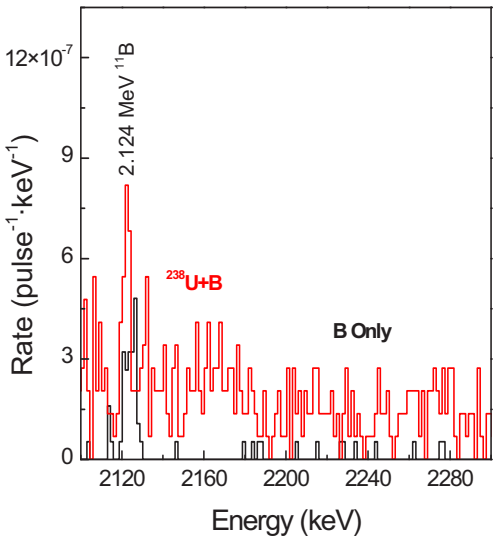

Figure 9. Gamma-ray spectra from a combined $^{11}B/^{238}U$ target (red line) and ^{11}B target (black line), irradiated with 3.0 MeV bremsstrahlung. The NRF transition from ^{11}B is labeled.

Table 1 compares the time averaged and pulse averaged rates from the combined target with that from only the boron target. The rates for the 2.124 ^{11}B NRF transition are consistent regardless of the presence of the ^{238}U target. The uncertainty associated with the combined target rate is larger due to the elevated background produced from the depleted uranium.

Table 1. Average rates for the 2.124 MeV ^{11}B NRF transition.

Target	2.124 MeV Time Averaged Rate (hr^{-1})	2.124 MeV Pulse Averaged Rate ($pulse^{-1}$)
B disk	8.5±1.5	$(2.6\pm0.5) \times 10^{-6}$
^{238}U + B	7.8±2.3	$(2.4\pm0.7) \times 10^{-6}$

Table 2. Time averaged background rates.

Target	2.124 MeV Background Rate (hr^{-1})	2.227 MeV Background Rate (hr^{-1})
^{238}U + B	7.7±0.46	4.9±0.8

Determining the average background rates for these data is more challenging due to the abundance of NRF transition lines in the region from 2.1 to 2.3 MeV. The 2.124 MeV peak from ^{11}B is present as should be peaks at 2.131, 2.164, **2.176**, 2.200, **2.209**, **2.245**, 2.250, and 2.295 MeV from ^{238}U (the energies listed in bold are expected to be the strongest transitions). Hence, many of the regions in Figure 9 that would be used for determining the background actually contain NRF transition peaks; using these regions for determining the background would have overestimated the actual background. Therefore, the rates shown in Table 1 have been background subtracted via a sideband subtraction technique. These sideband regions spanned from 2.068 to 2.118 MeV for the lower band and 2.131 to 2.235 MeV for the upper band. This may also have overestimated the background under the 2.124 MeV ^{11}B NRF peak, thereby causing an underestimation of the rate. Nevertheless, the calculated background rate under the 2.124 MeV line is shown in Table 2.

4. NRF MEASUREMENTS AT 900 HZ

It was obvious that employing a significantly thinner high-Z target allowed for much easier identification of the NRF transitions with relatively small integrated cross sections. As has been mentioned previously, there was approximately the same number of nuclei in the ^{238}U and ^{11}B targets. However, the areal dimensions of the ^{238}U target were larger than the beam spot, resulting in a smaller effective number of nuclei being irradiated. Therefore, it was determined that a substantially longer data collection time, in conjunction with an increased repetition rate, was necessary to achieve a statistical certainty with the ^{238}U transitions comparable with that from the ^{11}B transition.

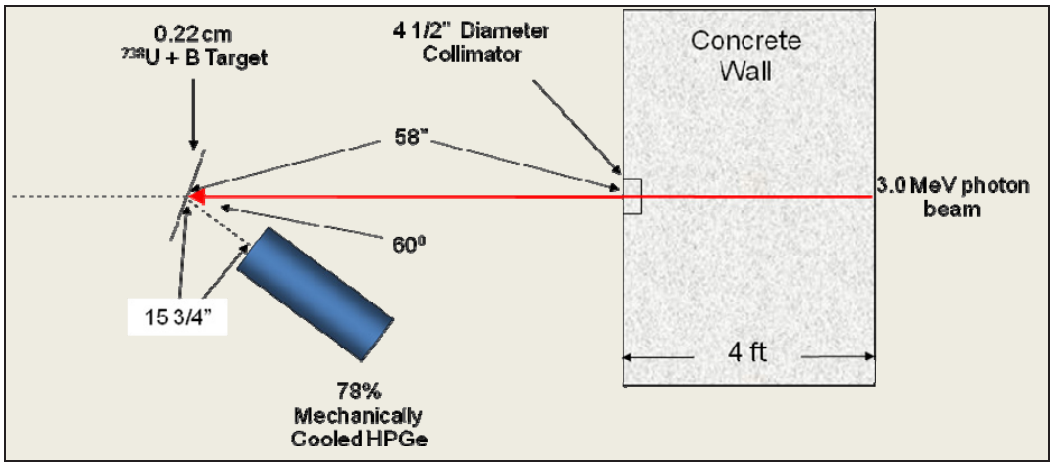

Figure 10. Schematic representation of the experimental setup used for the NRF measurements.

Figure 10 shows a schematic representation of the general experimental setup used during this research. A target comprised of a 10.16 cm square, 0.216 cm thick depleted uranium plate and a 5.08 cm diameter, 0.635 cm thick boron disk was utilized. The accelerator was operated with a repetition rate of 900 Hz and produced a ~3 MeV endpoint energy bremsstrahlung beam. The detector was gated on for 35.8 μs after the accelerator pulse, which was dictated mostly by the width of the detector's amplified pulses. For this experiment, data were collected continuously for a ~54 hour period (data was only collected during the bremsstrahlung pulses). Figure 11 shows the data collected during the experiment. Included in the plots are different gamma-ray lines of interest, as well as the 511 and 1022 keV lines from pair production, various background lines, and in the plot on the right the NRF transition lines, the majority of which exist between 2100 and 2300 keV. Again, the 2.124 MeV NRF transition from ^{11}B is readily identifiable. Although the ^{238}U NRF transitions may not be as pronounced as the boron transition, the 2.209 MeV transition is clearly present above the surrounding background and the 2.176 and 2.245 MeV lines appear promising.

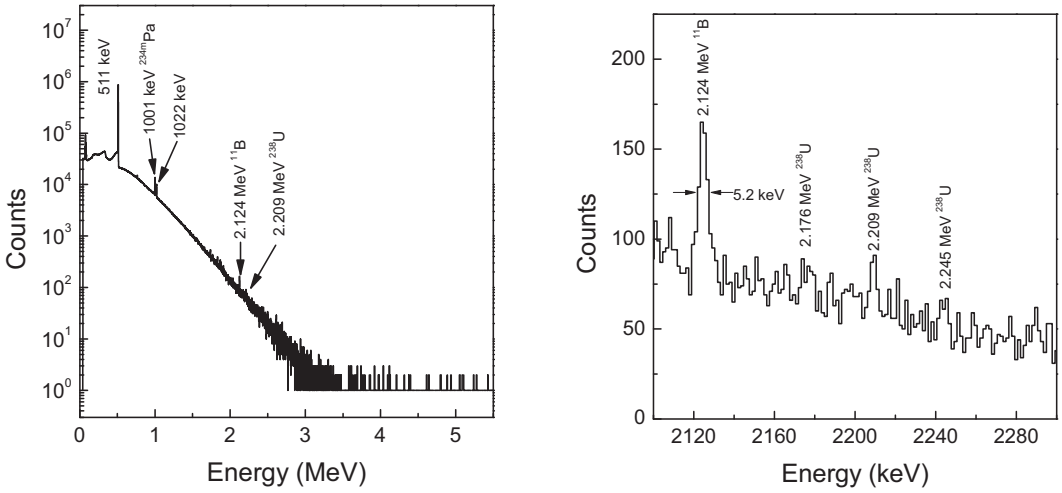

Figure 11. Gamma-ray spectra collected during irradiation of a ^{238}U and ^{11}B target. The plot on the left shows the complete spectra, while the plot at right shows a selected region containing NRF transitions of interest.

4.1 Passive Background Subtraction

It was well understood at this point that the background, both active and passive, can greatly diminish the ability to effectively identify NRF transitions in the presence of naturally radioactive and/or high-Z materials. As a result, a more in depth characterization of the background was sought. Figure 12 presents passive background gamma-ray spectra collected both with and without the ^{238}U and ^{11}B targets present. Because of the natural ^{238}U decay chain, the passive background below ~2 MeV is substantially higher with the target present than without. Conversely, for gamma-ray energies above 2 MeV, the passive backgrounds are comparable, suggesting this region is dominated by the radioactivity of the environment. Particular attention should be paid to the strong presence of the 2.205 MeV peak, as this is very close to where the 2.209 MeV ^{238}U NRF transition is expected. At this time, the source of this gamma-ray peak is undetermined.

To subtract the passive background from the active NRF data, the passive data need to be scaled accordingly. The passive data were collected continuously, whereas the NRF data were only collected during the bremsstrahlung pulses. Hence, the passive data were scaled according to

$$\Delta t_{live} = \Delta t_{run} \cdot f_a \cdot \delta t_{gate}, \tag{11}$$

where Δt_{live} is the experiment run time, f_a is the accelerator repetition rate, and δt_{gate} is the gate width. The results of the background subtraction are presented in Figure 13. The black data represent the active gamma-ray spectra, the blue data are the passive background, and the red data are the passive background-subtracted data. By performing this subtraction the effects of ^{234m}Pa, the ^{238}U decay chain, and ^{208}Tl are essentially eliminated from the active data set.

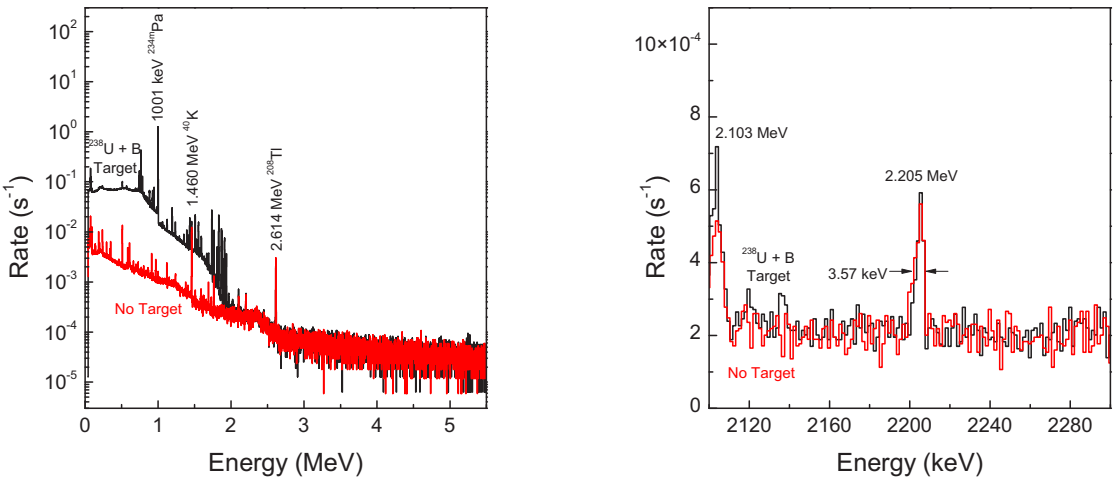

Figure 12. Passive background gamma-ray spectra from with the ^{238}U and ^{11}B target (black data) and without the target present (red data). The plot on the left shows the complete spectra, while the plot on the right shows a selected region where the NRF transitions of interest should appear during irradiation.

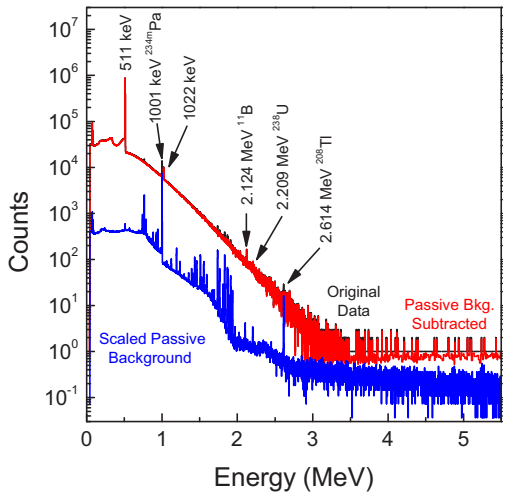

Figure 13. Passive background gamma-ray spectra and passive background-subtracted spectra. Subtracting the passive background effectively eliminates the presence of gamma-rays emitted by ^{234m}Pa, the ^{238}U decay chain, and ^{208}Tl.

4.2 Active Background Subtraction

While subtracting the passive background was fairly straightforward, characterizing and subtracting the active background required an alternative approach. Ideally, the active baseline could be subtracted by using simple sideband subtraction. However, performing sideband subtraction requires regions near the peak(s) to be identified as consisting of true background. This is non-trivial in the region of interest for ^{238}U transitions due to the large abundance of gamma-ray lines from both primary NRF transitions at 2.176, 2.209, and 2.245 MeV and secondary transitions at 2.131, 2.164, 2.200, 2.250, and 2.295 MeV (see Figure 14). Each of the secondary transitions occurs when a primary excited state de-excites to the first

excited state of ^{238}U at 44.916 keV, with the exception of the 2.295 MeV line. The 2.295 MeV line is a result of a direct transition from the 2.295 MeV excited state to the ground state of ^{238}U; however, because the width of this level is 5 times smaller than the 2.176 or 2.209 MeV levels, it will be treated here as a secondary transition.

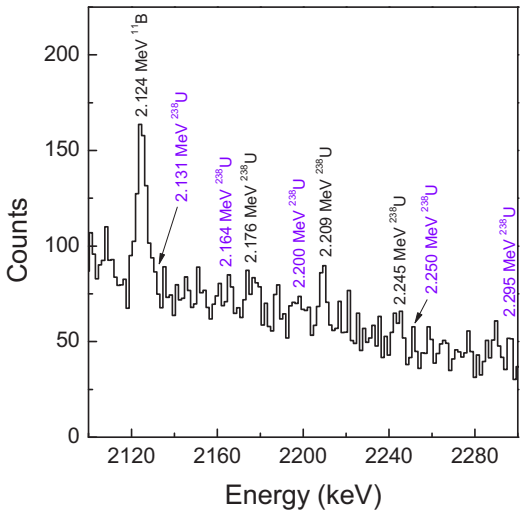

Figure 14. General region of interest for ^{238}U NRF transitions. The large abundance of lines from both primary and secondary transitions makes sideband subtraction challenging in this region.

As can be seen in Figure 15, the number of counts appears to decrease exponentially as a function of increasing energy from ~1.5 to ~3 MeV. Therefore, an exponential function was fit to the data from 1.766 to 2.678 MeV, which can be seen as the red line in Figure 15. The parameters for the fitting function Ae^{-BE}, where E is the gamma-ray energy, are shown in Table 3. With these parameters, the R-squared value for the fit is 0.982 over the range 1.766 to 2.678 MeV, indicating the fit correctly describes the behavior of 98% of the data. It should be noted, however, that the fitting routine did not weight the data by the corresponding uncertainty.

Table 3. Parameters for the fitting function Ae^{-BE}.

Parameter	Fit Value
A	$(4.1\pm0.3) \times 10^{5}$
B	$(4.00\pm0.03) \times 10^{-3}$ keV^{-1}

In addition to verifying the qualitative representation of the baseline provided by the fit, additional verification was performed to ensure the fit represented the baseline quantitatively as well. For this, regions are needed that are void of NRF transition lines so that the yield per channel (i.e., counts per channel) from the data can be compared with the fit; if there is strong agreement, it can be assumed that the fit represents the baseline. Examining the ^{238}U NRF spectra presented by W. Bertozzi, et.al [2], the most attractive regions are between the 2.209 and 2.245 MeV NRF transition lines and between 2.301 and 2.359 MeV. Table 4 summarizes the yields in these regions from both the data and the exponential fit.

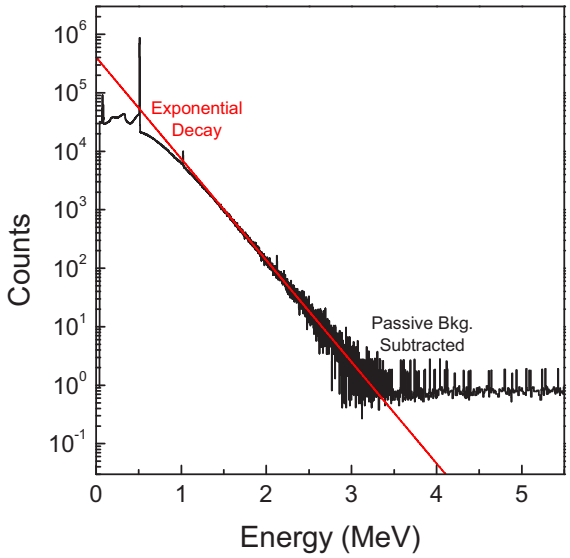

Figure 15. Passive background-subtracted gamma-ray spectrum (black data) with the resulting baseline (red data) generated from an exponential fit to the data.

Table 4. Yield summary for background regions.

Region	Data Yield per Channel	Fit Yield per Channel
2.214 to 2.240 MeV	55.0±1.7	54.9±1.2
2.301 to 2.359 MeV	36.19±0.96	36.46±0.57

There is strong agreement between the observed and fitted yields in these two background regions, indicating that the fit can be used for baseline subtraction. Therefore, the baseline generated from the fit was subtracted from the data, providing the counts above background, which is also the residual of the fit. If the exponential fit sufficiently represents the baseline, the residual should be randomly distributed around zero when there are no lines in the spectrum. Figure 16 shows the results of the baseline subtraction for two regions; the region containing the NRF transitions of interest are presented in Figure 17. There is a slight bowing in the residual between 1.780 to 1.980 MeV (left hand plot in Figure 16); however, this region contained a number of lines from the ^{238}U decay chain. The yield (or rates) of the various NRF transition lines can then be easily determined by simply summing around the peaks in the background and baseline subtracted spectra.

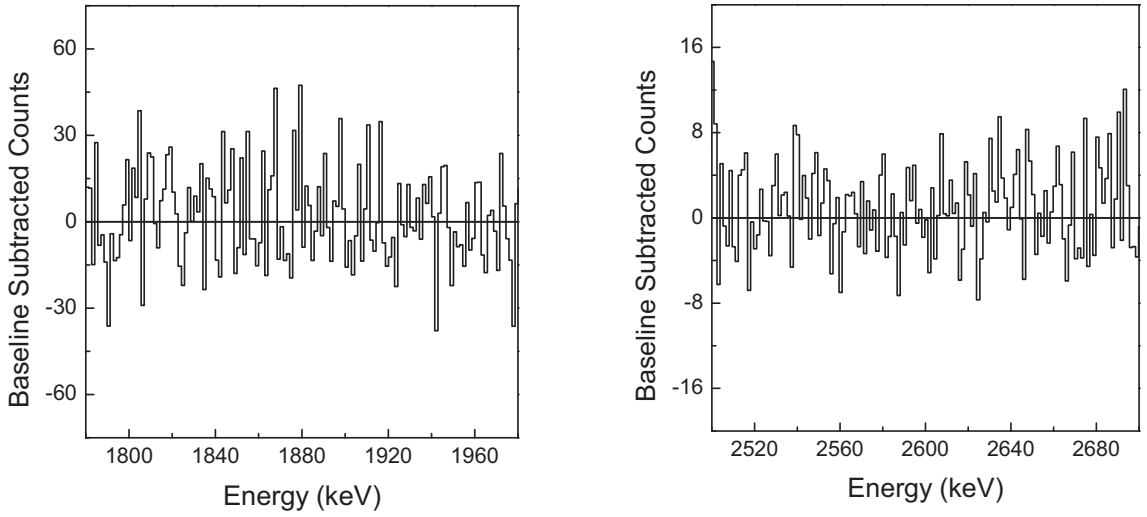

Figure 16. Residual plots for two energy regions; the region of the spectra containing the NRF transitions of interest will be shown in Figure 17.

4.3 Significance of NRF Transition Lines

Following the technique outlined by L. A. Currie [16], the significance of the various peaks in the spectrum was determined. The first consideration was how the net counts from the baseline (i.e., fully background subtracted) were obtained. The net baseline counts were calculated with

$$C_{net} = C_{Gr} - C_{PBkg} - C_{ABase}, \tag{12}$$

where C_{Gr} is the gross counts (i.e. the raw data), C_{PBkg} is the appropriately scaled passive background, and C_{ABase} is the active baseline from the exponential fit. The corresponding uncertainty is given by

$$\sigma_{net} = \sqrt{C_{Gr} + \left(\sigma_{PBkg}\right)^2 + \left(\sigma_{ABase}\right)^2}\ , \tag{13}$$

The critical decision level is given by

$$L_C = k\sigma_0, \tag{14}$$

where k sets the confidence level and σ_0 is the uncertainty in the background/baseline subtracted spectra when no NRF transition lines are present. It would be extremely challenging to acquire a target with background/baseline characteristics similar to the ^{238}U target, but void of the NRF transitions; the active baseline is strongly dependent on atomic number. If, theoretically, the NRF transition lines could be turned off without affecting the background/baseline, the gross spectrum counts would be

$$C_{0Gr} = C_{PBkg} + C_{ABase}, \tag{15}$$

and the net spectrum counts

$$C_0 = C_{0Gr} - C_{PBkg} - C_{ABase} = C_{PBkg} + C_{ABase} - C_{PBkg} - C_{ABase}, \tag{16}$$

which is zero. In such a spectrum, however, the fluctuations (i.e., the error) in the gross spectrum will be

$$\sqrt{C_{0G}} = \sqrt{C_{PBkg} + C_{ABase}} \quad , \tag{17}$$

and the error in the background/baseline subtracted spectrum is given by

$$\sigma_0 = \sqrt{C_{Pkg} + C_{ABase} + (\sigma_{PBkg})^2 + (\sigma_{ABase})^2} \quad . \tag{18}$$

Then, dividing the spectrum by σ_0 determines the significance of the data relative to the background/baseline. Figure 17 (left plot) shows the region of the spectrum over which the exponential fit was performed for the baseline subtraction. This region spans an energy range of 900 keV, corresponding to 638 total channels. Certainly, some number of excursions above the confidence levels not associated with NRF transition lines were expected. Table 5 compares these unexplained excursions with the expected number of excursions. The number of unexplained excursions seems to be reasonable compared to what was expected. As can be seen in the right plot in Figure 17, the confidence levels for the maximums of the 2.124 (^{11}B), 2.176, 2.209 and 2.245 MeV NRF transition lines are 100%, 96.8%, 99.9% and 95.6%, respectively.

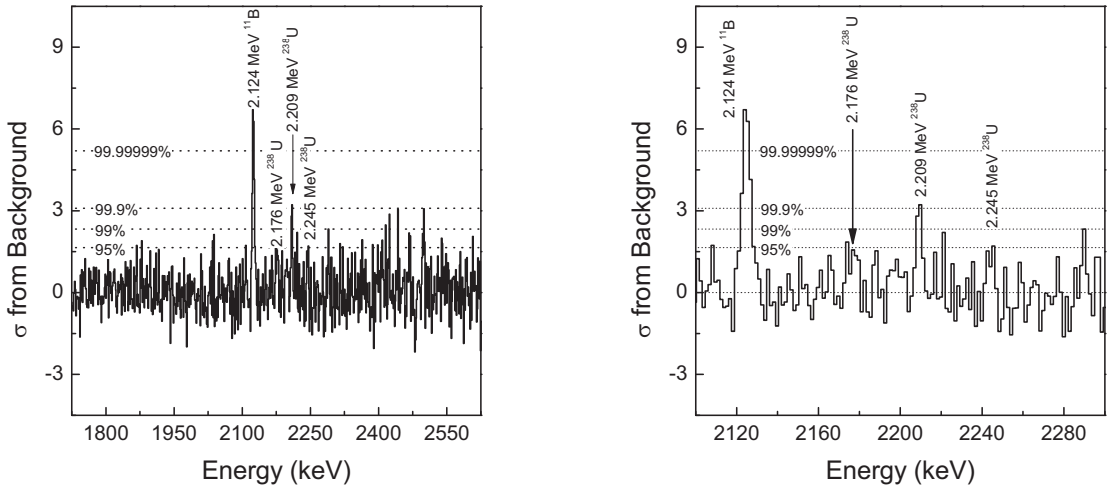

Figure 17. Statistical significance of the NRF transitions of interest.

Table 5. Summary of baseline excursions.

Confidence Level	Unexplained Excursions	Expected Excursions
50%	303	319
95%	31	31.9
99%	8	6.4
99.9%	0	0.64

4.4 NRF Transition Detection Rates and Ratios

Table 6. NRF transition rates from the 900 Hz data.

NRF Transition	Sum Window	Time Averaged Rate (hr-1)	Pulsed Averaged Rate (pulse-1)
2.124 MeV ^{11}B	1481–1488	5.79±0.71	(1.79±0.22) × 10^{-6}
2.176 MeV ^{238}U	1518–1523	1.36±0.50	(4.2±1.5) × 10^{-7}
2.209 MeV ^{238}U	1541–1546	1.45±0.47	(4.5±1.4) × 10^{-7}
2.245 MeV ^{238}U	1565–1570	0.59±0.41	(1.8±1.3) × 10^{-7}

At this point, it is straightforward to determine the total yield (i.e., counts) in any given peak simply by summing the baseline subtracted data. The error is given by the square root of the sum of the squares of the errors. The rates for the NRF transitions of interest are summarized in Table 5. The summed counts for the 2.124, 2.176, 2.209, and 2.245 MeV peaks are 9.2, 2.9, 3.3, and 1.47 times above σ_0, respectively. The rates for the 2.124 MeV NRF transition line from ^{11}B are compared in Figure 18 and appear to agree within errors.

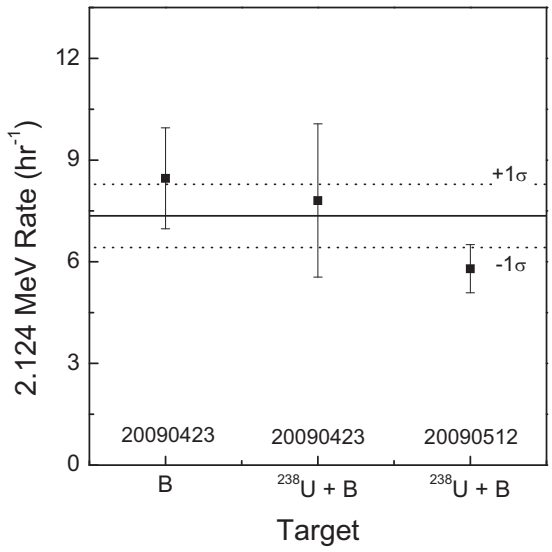

Figure 18. Comparison of the rates from the 2.124 MeV ^{11}B NRF transition.

The ratio of the ^{238}U NRF transition lines to the 2.124 MeV ^{11}B NRF transition line can now be calculated, assuming that only the bremsstrahlung intensity depends on position. The rate for NRF scattering is given by

$$R = f_{nrf}\left.\frac{d\Phi}{dE}\right|_{z=0} \int e^{\frac{-\left(x^2+y^2\right)}{2\cdot\sigma_{brm}^{\ 2}}}\, dA \cdot \int \frac{\sigma_{sc}(E)}{f_{nrf}\cdot\sigma_{ab}(E)+\sigma_e(E)} \cdot \left[1-e^{-n_t\cdot\left(f_{nrf}\cdot\sigma_{abs}(E)+\sigma_e(E)\right)\cdot z}\right] dE \quad , \tag{19}$$

where σ_{brm} is the spatial standard deviation of the bremsstrahlung intensity. The first integral is taken with respect to the area of the target and the intensity of the bremsstrahlung beam is assumed to be a two dimensional Gaussian. The ratio of any of the ^{238}U NRF transition lines to the 2.124 MeV NRF transition line from ^{11}B is then

$$\frac{R_{U_{NRF}}}{R_{2124}} = \frac{f_{U_{NRF}}}{f_{B_{11}}} \frac{\int_{A_U} e^{-\frac{r^2}{2\sigma_{brm}^2}} dA \int \frac{\sigma_{U_{NRF}}(E_\gamma)}{f_{U_{NRF}}\sigma_{U_{Abs}}(E_\gamma)+\sigma_{U_e}(E_\gamma)} \left(1-e^{-n_U[f_{U_{NRF}}\sigma_{U_{Abs}}(E_\gamma)+\sigma_{U_e}(E_\gamma)]z}\right) dE_\gamma}{\int_{A_B} e^{-\frac{r^2}{2\sigma_{brm}^2}} dA \int \frac{\sigma_{B_{NRF}}(E_\gamma)}{f_{B_{11}}\sigma_{B_{Abs}}(E_\gamma)+\sigma_{B_e}(E_\gamma)} \left(1-e^{-n_B[f_{B_{11}}\sigma_{B_{Abs}}(E_\gamma)+\sigma_{B_e}(E_\gamma)]z}\right) dE_\gamma} \quad (20)$$

where the subscript "U" or the "B" refers to uranium and boron, respectively. The ratio f_U/f_B can be solved and, using experimentally measured ratios with the calculated integrals, the consistencies of the ^{238}U NRF transition lines with the ^{11}B transition line can be verified. Figure 19 compares the ratios of ^{238}U NRF transitions to the ^{11}B transition. The calculated ratio is 1.248, as shown in the figure; while the measurements agree with this value, the uncertainties are relatively large.

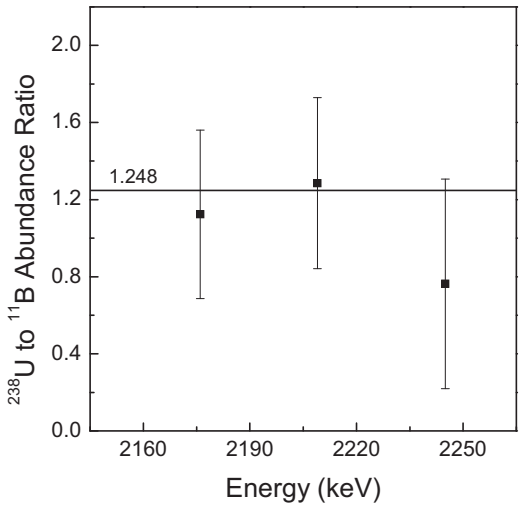

Figure 19. Comparison of the ^{238}U NRF transition rates to the 2.124 MeV ^{11}B NRF transition. The 1.248 ratio line represents the calculated ratio.

5. NRF MEASUREMENTS AT 3000 HZ

5.1 Multipulse Operations

As part of the primary tasking for FY 2009, the previously utilized, maximum repetition rate 1 kHz LINAC was modified to operate at a repetition rate in excess of 2 kHz. During FY 2008, this LINAC was modified to support up to 1 kHz repetition rates; one aspect of these modifications included decreases in the total capacitance and inductance of the pulse forming network. In contrast, for the FY 2009 modifications, capacitance and inductance were added to the pulse forming network and the RF driver was altered to operate with a wider pulse width. To further support repetition rates exceeding 2 kHz, the RF was injected at 300 Hz. Multiple-pulse electron gun control was realized with an upgraded electron gun hot deck operating with a burst mode pulsing system. Figure 20 shows the response of the beam monitor (blue data) and HPGe detector (black data) during initial multipulse operations. A ~20 μs RF pulse was injected with a repetition rate of 300 Hz, resulting in an approximately ~16 μs window in which an arbitrary number of electron pulses could be injected. While the electron pulse separation is 2 μs for the data shown in Figure 20, the electron pulse width, period (i.e., pulse separation), and amplitude can be selected by the user.

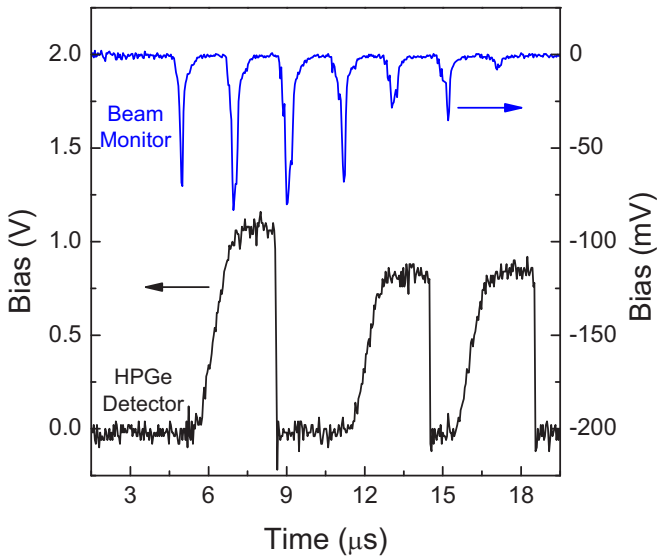

Figure 20. Beam monitor response (blue data) showing multipulse operations. The black data are output pulses from the HPGe detector, corresponding to individual bremsstrahlung pulses.

Figure 20 and Figure 21 also demonstrate a potential advantage and disadvantage of the multipulse operating mode. Using a high-speed, fixed conversion time analog-to-digital converter, multiple detector hits similar to those seen in Figure 20 can be processed, resulting in an effective bremsstrahlung repetition rate that is simply the number of electron pulses per RF pulse times the repetition rate of the RF pulse. Hence, the effective repetition rates were ~1.8 kHz and 2.4 kHz, respectively, for the data shown in Figure 20 and Figure 21. Figure 21 also demonstrates the effect of pulse pileup from two consecutive bremsstrahlung pulses. The effect can be eliminated by increasing the electron pulse separation, but at the expense of limiting the number of injected electron pulses. An advantage of the multipulse operation is an a priori understanding of when the pulse pileup would occur; it should be fairly straightforward to develop an algorithm to reject these pulses.

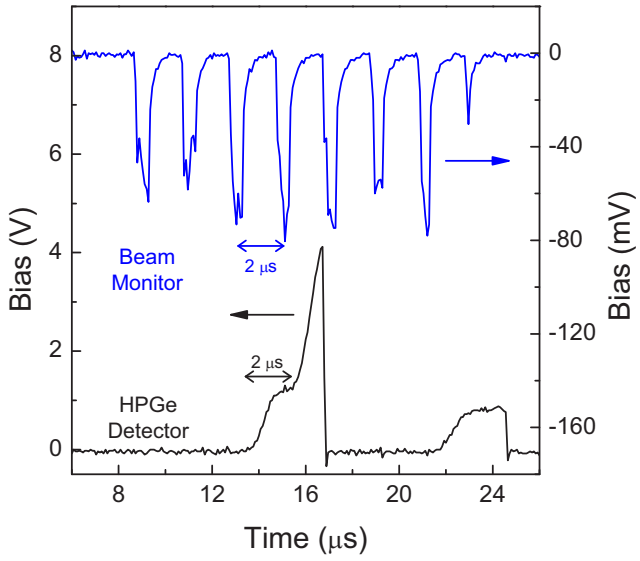

Figure 21. Multipulse operations with an effective repetition rate of 2.4 kHz. The blue data represent the response of the beam monitor, while the black data are from the HPGe detector. The black data also show the effect of pulse pileup from two consecutive bremsstrahlung pulses.

5.2 Experiments at 3 kHz

During each 16 μs RF pulse, 450 ns wide electron pulses were injected into the accelerator, separated by 1.6 μs, resulting in 10 electron/bremsstrahlung pulses per RF pulse. Hence, the effective bremsstrahlung repetition rate was 3 kHz; representative faraday cup and bremsstrahlung beam monitor traces from the oscilloscope are presented in Figure 22. As was the case for the 900 Hz measurements, the ^{238}U target was a 10.16 cm square, 0.21 cm thick depleted uranium plate. The boron disk had a 5.08 cm diameter and was 0.635 cm thick. The accelerator was operated at 3 MeV and the detector was gated on for 18 μs after the accelerator pulse, which was dictated mostly by the width of all 10 bremsstrahlung and the width of the amplified pulses coming from the detector. In these experiments a gated integrator amplifier was used that had a 3 μs shaping time.

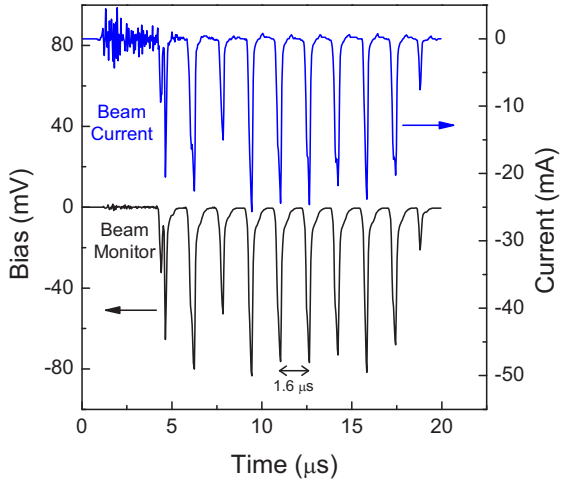

Figure 22. Faraday cup and beam monitor oscilloscope traces from the 3 kHz multipulse operations.

5.3 900 Hz and 3 kHz Rate Comparisons

The overall number of detected events per bremsstrahlung pulse decreased 30.9% from the 900 Hz measurements (0.11 hits per pulse) to the 3 kHz measurements (0.076 hits per pulse), primarily as a result of difficulties maintaining consistent charge per electron pulse. For gamma-ray energies below ~1.5 MeV, the detected photon rates decreased similarly, with a 38.7% decrease in the 511 keV rate and a 46.4% decrease in the 1022 keV rate (see Figure 23). It should be noted that both of these decreases are greater than the decrease in the detector hits per pulse. For gamma-ray energies above ~1.5 MeV, the detected photon rate actually increased at 3 kHz; in the background region between 2218 and 2238 keV, the rate increased by 26.9% (see Figure 24). This decrease in the low-energy region and increase in the high-energy region has two possible explanations. First, the pulse pileup has increased due to detector hits from at least two successive bremsstrahlung pulses within a single RF pulse. These events can be easily identified on an oscilloscope and their elimination should be straightforward using digitization techniques. Secondly, there was an increase in the collimator diameter from 1.27 cm for the 900 Hz experiment to 1.59 cm for the 3 kHz experiment. This change increased the effective area of the ^{238}U target in the beam, which would increase the high-energy yield relative to the low-energy yield. However, the beam spot measurements did not show any increases in the beam spot size. Hence, the pulse pileup appears to be the more plausible explanation. Of course, the rates (s^{-1}) are much larger for the 3 kHz data—approximately 4.23 times larger in the region between 2100 and 2300 keV.

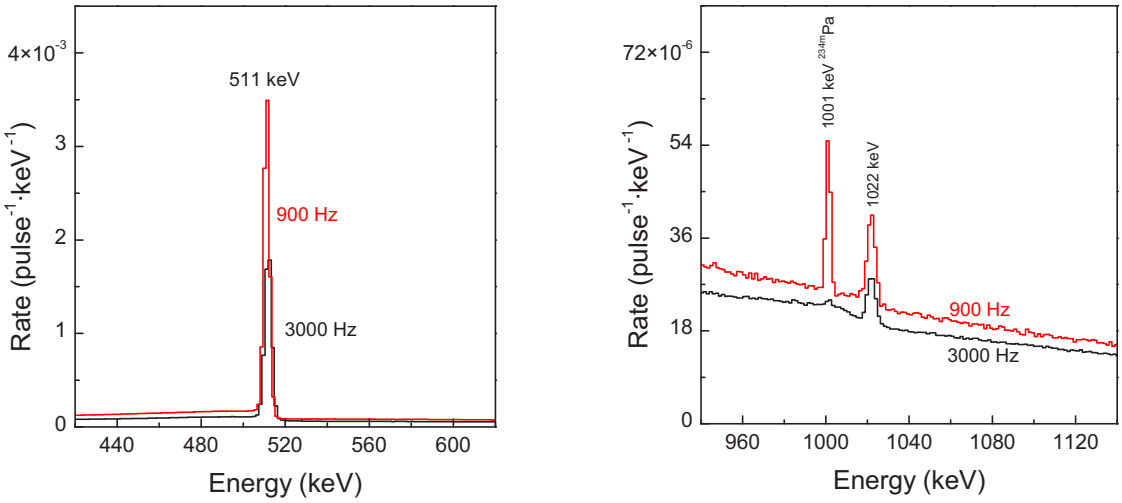

Figure 23. Comparison of detected gamma-ray rates from the 900 Hz and 3 kHz measurements.

The passive background peaks, which are evident in the 900 Hz experiment, are small to nonexistent in the 3 kHz experiment, as can be seen in Figure 24 (left plot). In the 900 Hz experiment, a 35.8 μs gate was used to enable the ADC, which was dictated by the 37 μs width of the amplified detector pulse. In contrast, the 3 kHz experiments used a 18 μs wide gate, which was dictated by the 16 μs wide RF pulse. Since a gated integrated amplifier was used that had a 3 μs shaping time, the amplified detector pulses were ~3.4 μs wide. The detector duty factor decreased from 3.2% in the 900 Hz experiment to 0.54% in the 3 kHz experiment, which is a factor of 5.96 decrease.

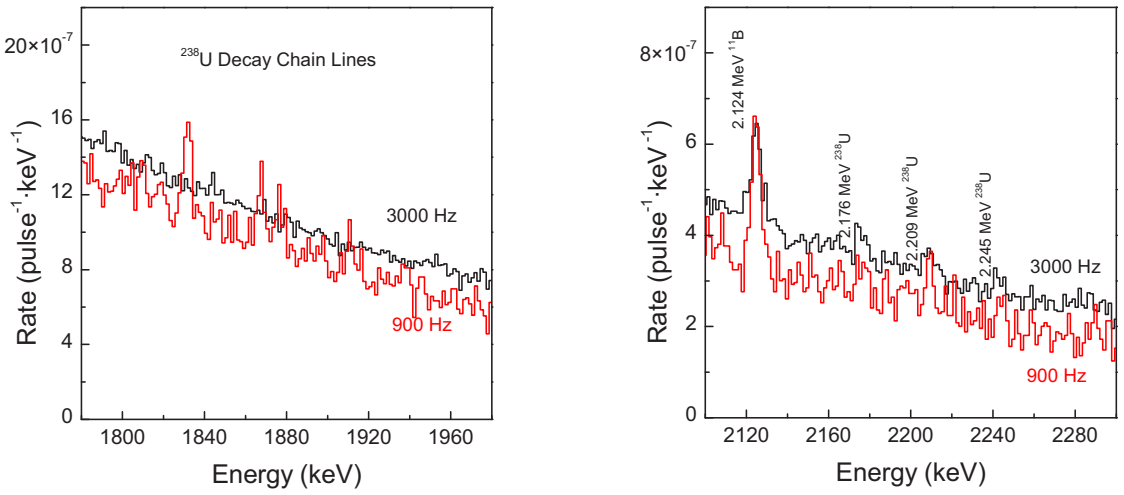

Figure 24. Comparison of detected gamma-ray rates from the 900 Hz and 3 kHz measurements.

5.4 Passive Background Subtraction

After concluding 3 kHz NRF measurements, a passive target background was collected. This background was essentially identical to the background taken after the 900 Hz experiments (see Section 4.1 Passive Background Subtraction) and has all the same background lines previously identified, including the unidentified line at ~2.205 MeV. As mentioned in the previous section, there is very little evidence of passive background in the original 3 kHz data because of the small detector duty factor (0.54%). Nevertheless, the passive background was subtracted from the original data to maintain consistency between the 900 Hz and 3 kHz data analyses. Details of the passive background scaling and subtraction are explained in Section 4.1 Passive Background Subtraction.

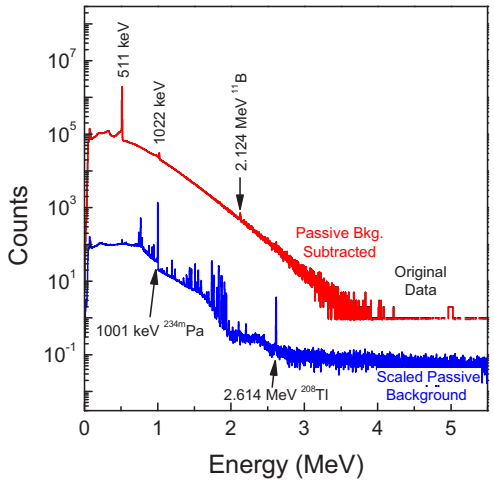

Figure 25. Passive background gamma-ray spectra and passive background-subtracted spectra from the 3 kHz measurements.

The passive background lines provide a means for examining how the energy resolution degraded when the spectroscopy amplifier (6 μs shaping time) was replaced with the gated integrator (3 μs shaping time). Table 7 summarizes the full width at half maximums (FWHM) measured for various lines. These include active lines (e.g., 511 keV from pair production), lines from the passive background (e.g., 2614 keV from ^{208}Tl), and the ^{11}B NRF transition line. For each gamma-ray energy measured, the FWHM is larger for the gated integrator (3 μs shaping time) than for the spectroscopy amplifier. In the high-energy region of interest for ^{238}U NRF transitions, the FWHM's have increased between 12% and 16%. There was one anomalous measurement for the unidentified 2205 keV line, which produced a FWHM of 3.57 keV using the spectroscopy amplifier. Additionally, a 2.617 MeV peak was observed in the data. Initially, this was attributed to the 2.614 MeV ^{208}Tl line and a slight imprecision with the energy calibration. However, the NRF transition lines and the electron-positron annihilation lines suggest that the calibration is correct. Furthermore, the calibration spectra collected before and after the experiment support the calibration as well. This, coupled with the fact that the passive background is too small to allow the 2.614 MeV line from ^{208}Tl to contribute to the active measurements, leaves the source of this line undetermined.

Table 7. Comparison summary for the FWHM of various background lines collected with the two amplifiers.

	FWHM	
Energy and Source	Gated Integrator 3 μs Shaping Time (keV)	Spectroscopy Amplifier 6 μs Shaping Time (keV)
511 keV e^+/e^- Annihilation	3.85	3.03
1001 keV ^{234m}Pa	3.26	2.69
1022 keV e^+/e^- Annihilation	6.26	4.54
1831 keV ^{238}U Decay Chain	4.94	4.42
2124 keV ^{11}B NRF Transition	6.04	5.20
2205 keV Unidentified Background	6.59	3.57
2614 keV ^{208}Tl	6.45	5.71

5.5 Active Background Subtraction

Similar to the 900 Hz measurements, the active background (i.e., the baseline) was determined by performing an exponential fit to the region of data between 1.766 and 2.678 MeV, corresponding to channels 1202 and 1822. The NRF transition lines at 2.124, 2.176, 2.209, and 2.245 MeV were not included in the fit, as this would have produced an overestimation of the baseline. The parameters for the fitting function Ae^{-BE}, where E is the gamma-ray energy, are shown in Table 8.

Table 8. Parameters for the fitting function Ae^{-BE}.

Parameter	Fit Value
A	$(1.119\pm0.03) \times 10^{6}$
B	$(3.66\pm0.01) \times 10^{-3}$ keV^{-1}

With these parameters, the R-squared value for the fit is 0.998, excluding the NRF transition lines. Hence, the fit appears to accurately represent the baseline. Table 9 compares the actual yield per channel and the yield per channel expected from the fit for energy regions between 2032 and 2104 MeV, 2.209 and 2.245 MeV (^{238}U NRF transition lines), and 2.301 and 2.358 MeV. The agreement in these background

regions is reasonable; however, the data yield for the region between 2.218 and 2.238 MeV is 1.4 standard deviations below the fit baseline.

Table 9. Yield summary for background regions.

Region	Data Yield Per Channel	Fit Yield Per Channel
2.032 to 2.104 MeV	579.8±3.4	579.8±2.7
2.218 to 2.238 MeV	314.9±4.6	322.5±2.9
2.301 to 2.359 MeV	222.5±2.4	222.3±1.2

The exponential baseline was subtracted from the data, leaving the counts above background, which is also the residual of the exponential fit. If this fit represents the baseline, the residual should be randomly distributed about zero in regions containing only background counts. Figure 26 shows baseline subtracted data for two energy regions. In addition to the 2.176, 2.209, and 2.245 MeV ^{238}U NRF transition lines, which are clearly identifiable, and the 2.124 MeV ^{11}B NRF transition line, a line at 1.846 MeV appears to be present as well. This peak, which was not observed during previous measurements, is an additional ^{238}U NRF transition with an integrated cross section of 23 b·eV.

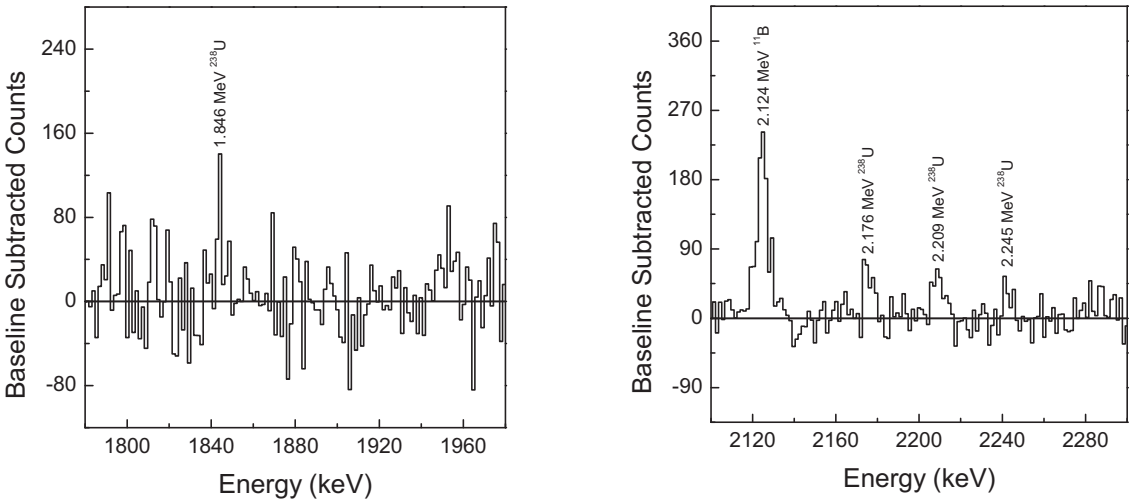

Figure 26. Residual plots for two energy regions. The ^{11}B and ^{238}U NRF transition lines are clearly identifiable.

5.6 Significance of NRF Transition Lines

Figure 27 (left plot) shows the region over which the exponential fit was performed for the baseline subtraction; there are a number of channels that cross the various confidence levels. However, with a large number of channels, we would expect excursions above the confidence levels that are not associated with NRF transition lines. Table 10 summarizes the unexplained excursions, excluding the channels associated with the 2.124, 2.176, 2.209, and the 2.245 MeV NRF transitions.

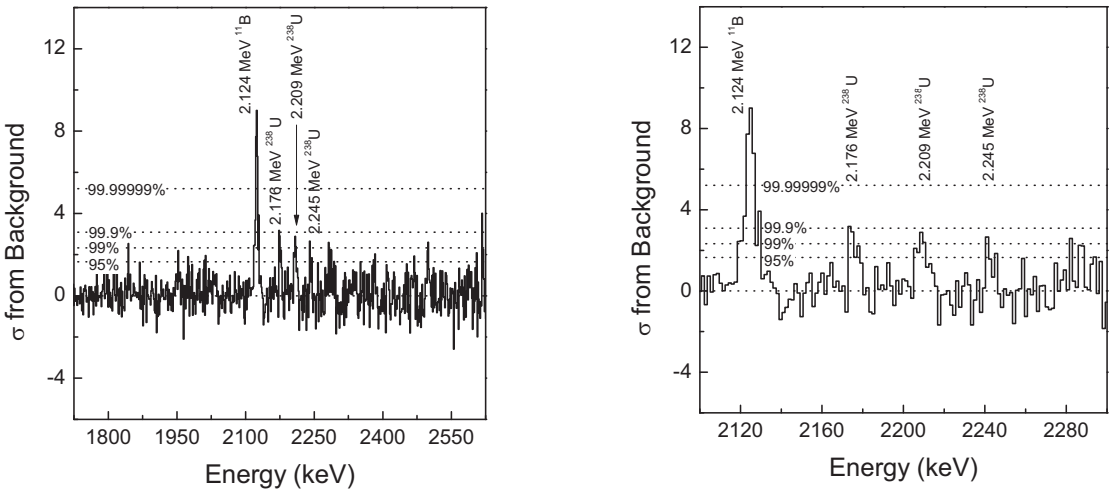

Figure 27. Statistical significance of the NRF transitions of interest. The plot at left shows the region over which the exponential fit was performed for the baseline subtraction. The plot at right shows a selected region containing the NRF transitions of interest.

Table 10. Summary of baseline excursions.

Confidence Level	Unexplained Excursions	Expected Excursions
50%	270	297
95%	22	29.7
99%	5	5.9
99.9%	1	0.59

The number of unexplained excursions is fairly reasonable compared to what was expected. The one unexplained excursion above the 99.9% confidence level is from the unidentified "line" at 2.617 MeV. There is also an excursion above the 99% confidence level at ~2.500 MeV, which was also present in the 900 Hz data. The confidence levels for the maximums of the 2.124, 2.176, 2.209, and 2.245 MeV NRF transition lines are 100%, 99.9%, 99.8% and 99.6%, respectively. Details regarding the calculations are presented in Section 4.3 Significance of NRF Transition Lines.

5.7 NRF Transition Detection Rates and Ratios

As with the 900 Hz measurements, the total yield (i.e., counts) in any given peak can be determined by summing the baseline subtracted data. The uncertainty is the square root of the sum of the squares of the errors. Table 11 summarizes the rates; the respective summed counts are 12.4, 3.7, 4.6, and 2.1 times above σ_0. The ratio of the ^{238}U NRF transition lines to the 2.124 MeV ^{11}B NRF transition was then calculated in the same manner as with the 900 Hz data. Details regarding the calculations can be found in Section 4.4 NRF Transition Detection Rates and Ratios. Figure 28 compares the ratios of ^{238}U NRF transitions to the ^{11}B transition. The calculated ratio is 1.248, as represented by the solid line in the figure; while the measurements agree with this value, the uncertainties are relatively large.

Table 11. NRF transition rates from the 3000 Hz data.

NRF Transition	Sum Window	Time Averaged Rate (hr^{-1})	Pulsed Averaged Rate ($pulse^{-1}$)
2.124 MeV ^{11}B	1440–1449	15.2±1.3	$(1.41\pm0.12) \times 10^{-6}$
2.176 MeV ^{238}U	1478–1485	3.53±0.99	$(3.27\pm0.92) \times 10^{-7}$
2.209 MeV ^{238}U	1500–1507	4.10±0.93	$(3.79\pm0.86) \times 10^{-7}$
2.245 MeV ^{238}U	1523–1530	1.78±0.84	$(1.65\pm0.78) \times 10^{-7}$

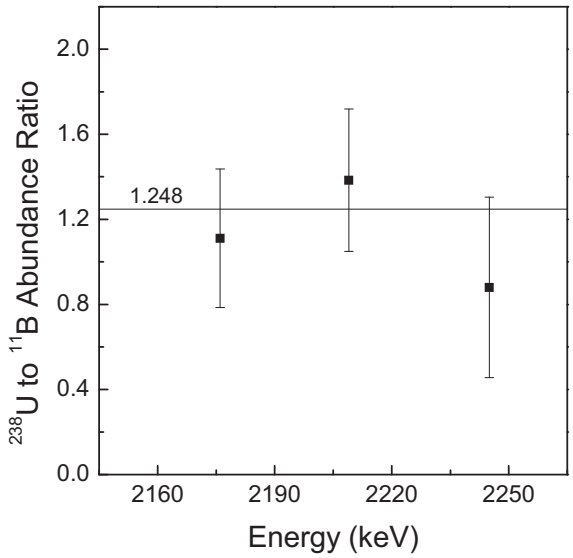

Figure 28. Comparison of the ^{238}U NRF transition rates to the 2.124 MeV ^{11}B NRF transition. The line corresponding to a ratio of 1.248 represents the expected ratio.

5.8 3 kHz versus 900 Hz Rate Comparisons

Figure 29 shows the background subtracted rates in terms of per unit time (left plot) or per accelerator pulse (right plot). The rate per hour is significantly larger for the 3 kHz data as would be expected. The rates per bremsstrahlung pulse are a bit smaller for the 3 kHz data primarily due to difficulties in maintaining a consistent accelerator tune across each electron pulses in a RF pulse. Table 12 and Table 13 summarize these rate data. Figure 30 shows the fractional rate increases (i.e., R_{3kHz}/R_{900Hz}) for the total rates for the 2.124 (^{11}B), 2.176, 2.209, and 2.245 MeV NRF transition lines. As expected, the overall per pulse rates at 3 kHz were generally consistent with those observed at 900 Hz. The rates per hour increased significantly with the 3 kHz repetition rate, to within a standard deviation of the expected increase of a factor of 3.3; however, the uncertainties are relatively large. Finally, Figure 31 illustrates the enhanced NRF capability, given as a per hour rate, of the multipulse operations (3 kHz repetition rate). These data have not been baseline subtracted, although the baselines are shown (red lines). While the 2.124 MeV transition is clearly identifiable for both data sets, the ^{238}U transitions are essentially unrecognizable in the 900 Hz data. However, the presence of these lines in the 3 kHz data is statistically significant, with confidences of 100%, 99.99%, 100%, and 98.21%. This result is a 37% increase in statistical confidence over the 900 Hz measurements.

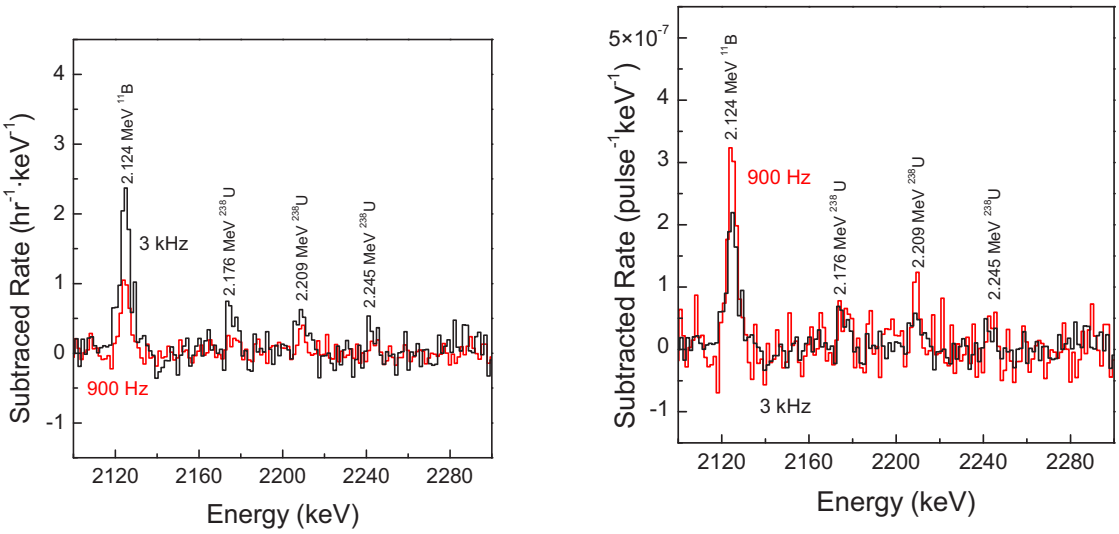

Figure 29. Per hour and per pulse rate comparisons between the 900 and 3000 Hz measurements. The regions shown contain the ^{238}U and ^{11}B NRF transitions of interest.

Table 12. Summary of per hour rates for the NRF transitions of interest.

Time Averaged Rate (hr^{-1})		
NRF Transition	3000 Hz 06-08-2009	900 Hz 05-12-2009
2.124 MeV ^{11}B	15.2±1.3	5.79±0.71
2.176 MeV ^{238}U	3.53±0.99	1.36±0.50
2.209 MeV ^{238}U	4.10±0.93	1.45±0.47
2.245 MeV ^{238}U	1.78±0.84	0.59±0.41

Table 13. Summary of per electron pulse rates for the NRF transitions of interest.

Pulse Averaged Rate ($pulse^{-1}$)		
NRF Transition	3000 Hz 06-08-2009	900 Hz 05-12-2009
2.124 MeV ^{11}B	$(1.41\pm0.12)\times10^{-6}$	$(1.79\pm0.22)\times10^{-6}$
2.176 MeV ^{238}U	$(3.27\pm0.92)\times10^{-7}$	$(4.2\pm1.5)\times10^{-7}$
2.209 MeV ^{238}U	$(3.79\pm0.86)\times10^{-7}$	$(4.5\pm1.4)\times10^{-7}$
2.245 MeV ^{238}U	$(1.65\pm0.78)\times10^{-7}$	$(1.8\pm1.3)\times10^{-7}$

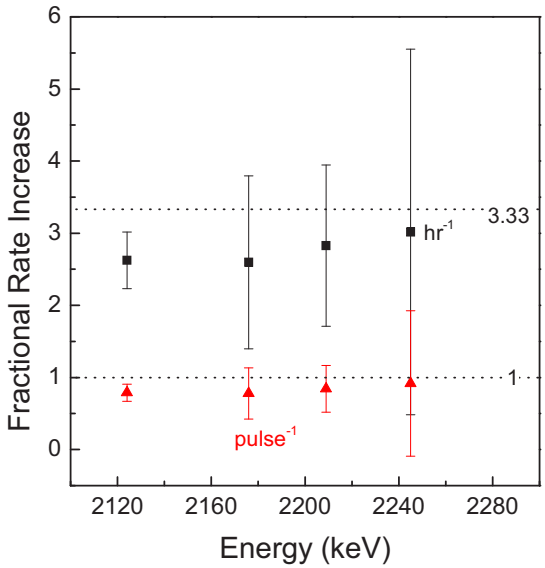

Figure 30. Fractional rate increase of the 3 kHz data over the 900 Hz data for the ^{238}U and ^{11}B NRF transitions. The rates were not expected to vary per pulse; however, an increase of 3.33 was expected based on the increased effective repetition rate.

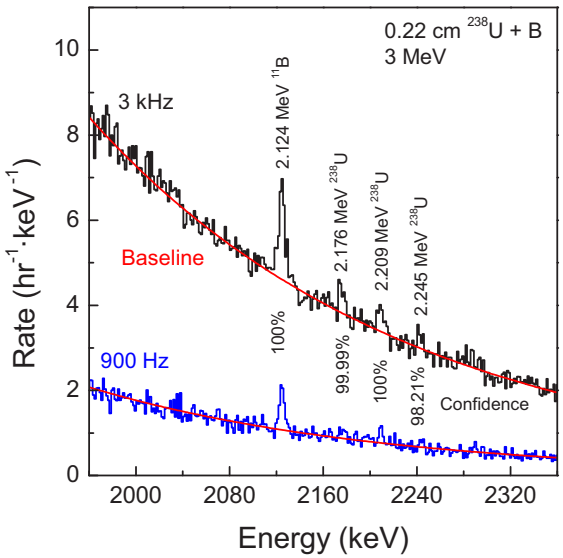

Figure 31. Comparison of the 3 kHz and 900 Hz data, without baseline subtraction. The red lines represent the respective baselines. This comparison strongly highlights the enhanced NRF performance at 3 kHz.

6. EXPENDITURES

A total of $950,000 was funded and budgeted for the FY 2009 effort. A contract was written to the Idaho Accelerator Center for $548,000 to accommodate accelerator modifications and to fund needed engineering labor as well as scientific collaboration. Figure 31 and Table 14 show the combined monthly expenditures by the INL and the IAC.

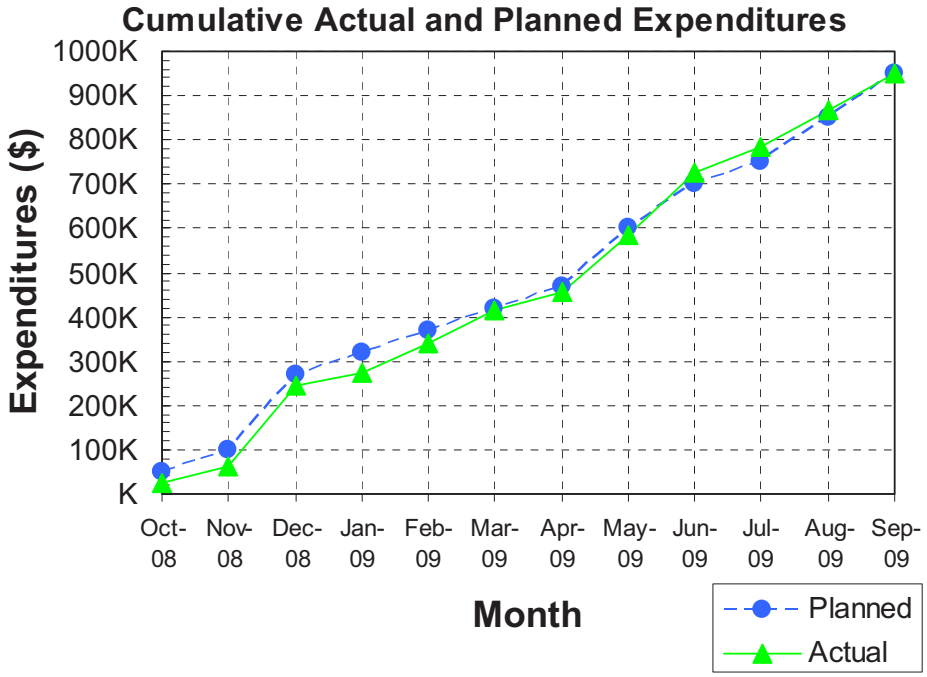

Figure 31. Combined planned and actual monthly expenditures by INL and IAC.

Table 14. Monthly breakdown of experimental versus monthly expenditures.

Date	Actual in Period ($)	Cumulative Actual	Planned for Period ($)	Cumulative Planned
October 1, 2008	26,469	26,469	56,042	50,000
November 1, 2008	37,568	64,037	56,042	100,000
December 1, 2008	179,854	243,891	56,042	270,000
January 1, 2009	28,568	272,459	148,375	320,000
February 1, 2009	69,859	342,318	148,375	370,000
March 1, 2009	74,587	416,905	125,875	420,000
April 1, 2009	38,687	455,592	155,875	470,000
May 1, 2009	127,594	583,186	155,875	600,000
June 1, 2009	145,000	728,186	117,500	700,000
July 1, 2009	56,000	784,186	30,000	750,000
August 1, 2009	82,907	867,093	50,000	850,000
September 1, 2009	82,907	950,000	50,000	950,000

7. CONCLUSIONS

The FY 2009 effort continued to assess the applicability of a variable repetition rate, pulsed bremsstrahlung beam to NRF measurements. During FY 2008, the data acquisition system was substantially affected by RF pickup, which was generated by the accelerator control system. To minimize this noise, several components of the detector and associated hardware were modified, to include a differential output capability for the HPGe detector and single-run, double shielded signal cables for data acquisition. Ground loops were effectively eliminated through electrical isolation of the acquisition system from the accelerator control system. The LINAC gun trigger signal was passed to an electrical-to-optical converter and fiber optics carried the resulting signal to the acquisition system, where the signal was converted from an optical signal back to an electrical signal. Overall, the RF noise pickup in the acquisition system was reduced by a factor of more than 100.

Calculations for the NRF yield as a function of increasing target thickness strongly suggested the use of a thinner ^{238}U target. Hence, a 0.216 cm thick depleted uranium plate was combined with a 0.635 cm thick boron disk for subsequent measurements. At the time of the measurement, the data collected with a LINAC repetition rate of 900 Hz represented the most definitive identification of a relatively small integrated cross section NRF transition (~52 b·eV) in the presence of a high-Z material. Although the ^{238}U NRF transitions (2.176 and 2.209 MeV) were not as clearly visible as expected, the 2.124 MeV ^{11}B transition was clearly present, well above background. The total number of nuclei from each isotope in the target was comparable, with 1.35×10^{24} ^{11}B nuclei and 1.193×10^{24} ^{238}U nuclei in the target. Because the areal dimensions of the depleted uranium plate were larger than the bremsstrahlung beam spot, follow-on measurements utilized a consistent methodology with increased data collection time to compensate. The result was successful identification of both ^{11}B and ^{238}U transitions, with confidence levels of 100% (2.124 MeV ^{11}B), 96.8% (2.176 MeV), 99.9% (2.209 MeV), and 95.6% (2.245 MeV).

As part of the primary tasking for FY 2009, the LINAC was modified to support up to 3 kHz repetition rates. Capacitance and inductance were added to the pulse forming network and the RF driver was changed to support longer pulse widths. An upgraded electron gun hot deck with a burst mode pulsing system enabled multiple-pulse electron gun control. By injecting a ~20 μs wide RF pulse with a 300 Hz repetition rate, and pulsing the electron gun up to 10 times within each RF pulse, the effective electron/bremsstrahlung repetition rate of the LINAC was 3 kHz. Measurements with the increased repetition rate capability were superior to any of the previous efforts. The ^{238}U NRF transitions of interest were detected with statistical significances of 99.99% (2.176 MeV), 100% (2.209 MeV), and 98.21% (2.245 MeV). Overall, measurements performed at 3 kHz produced a 37% increase in statistical confidence over the 900 Hz measurements.

8. REFERENCES

1. U. Kneissl, H. H. Pitz, and A. Zilges, *Prog. Part. Nucl. Phys.* **37**, 349 (1996).
2. W. Bertozzi and R. J. Ledoux, *Nucl. Instr. and Methods* B **241**, 820 (2005).
3. W. Bertozzi, S. E. Korbly, R. J. Ledoux, and W. Park, *Nucl. Instr. and Methods* B **261**, 331 (2007).
4. J. L. Jones, et al., "Pulsed Photonuclear Assessment (PPA) Technique: CY04 Year-end Progress Report," Formal Report, INL 05-02583, February 2005.
5. D. R. Norman, J. L. Jones, B. W. Blackburn, K. J. Haskell, J. T. Johnson, S. M. Watson, A. W. Hunt, R. Spaulding and F. Harmon, *Nucl. Instr. and Methods* B **261**, 316 (2007).
6. J. L. Jones, *SPIE Proceedings* **2867**, 202 (1996).
7. T. R. Twomey, A. J. Caffrey and D. L. Chichester, "Nondestructive Identification of Chemical Warfare Agents and Explosives by Neutron Generator-Driven PGNAA," INL Report, INL/CON-07-12304, February 2007.
8. "Better Than Dogs," *Need to Know*, INL National Security Newsletter **3**, 2, 6 (January 2003).
9. M. T. Kinlaw, et al., "High Repetition Rate, LINAC-Based Nuclear Resonance Fluorescence," Formal Report, INL/EXT-08-15116, December 2008.
10. M. T. Kinlaw and A. W. Hunt, *Appl. Phys. Lett.* **86**, 254104 (2005).
11. M. T. Kinlaw and A. W. Hunt, *Nucl. Instr. and Methods* A **562**, 1081 (2006).
12. J. L. Jones, et al., "Proof-of-Concept Assessment of a Photofission-based Interrogations System for Detection of Shielded Nuclear Material," Formal Report, INEEL-2000-01523, November 2000.
13. J. L. Jones, et al., *Nuclear Instruments and Methods in Physics Research* A **562**, 1085 (2006).
14. J. L. Jones, B. W. Blackburn, S. M. Watson, D. R. Norman and A. W. Hunt, *Nucl. Instr. and Methods* B **261**, 326 (2007).
15. F. R. Metzger, *Prog. Nucl. Phys.* **7**, 53 (1959).
16. L. A. Currie, *Analyt. Chem*. **40**, 586 (1968).